Electronic Supplementary Material (ESI) for New Journal of Chemistry.
This journal is © The Royal Society of Chemistry and the Centre National de la Recherche Scientifique 2023

Electronic Supplementary Material (ESI) for New Journal of Chemistry.
This journal is © The Royal Society of Chemistry and the Centre National de la Recherche Scientifique 2022

Supporting Information

Nitrogen–rich hierarchical porous carbon nanoscrolls with atomically dispersed Co sites for enhanced oxygen reduction reaction and lithium ion batteries

*Ziyan Wen [1, a], Yangyang Chen[1, a, b], Da Hu[a], Binhong He[a], Minjie Zhou[a]**

a Key Laboratory of Hunan Province for Advanced Carbon–based Functional Materials, School of Chemistry and Chemical Engineering, Hunan Institute of Science and Technology, Yueyang 414006, Hunan, China

b College of Materials Science and Technology, Central South University of Forestry and Technology, Changsha 410004, China.

***Corresponding authors.**

Email addresses: zmj0104@126.com (M. Zhou)

1 These authors contributed equally to this work.

Figure S1-S12, **Table S1-S8**

1. Experimental section

1.1 Chemicals and materials

All reagents were of analytical grade and used as received without further purification. Pyrrole (98%) and $Co(NO_3)_3 \cdot 6H_2O$ were purchased from Sigma–Aldrich Co., Ltd. Urea (99%) was bought from Shanghai Aladdin Biochemical Technology Co., Ltd. Ammonium persulphate (≥98%) was bought from Shanghai Shiyicr Co., Ltd. Ultrapure water was used in this study.

1.2 Synthesis of Co–CN–*m*

Co–doped g–C_3N_4 (Co–CN) was synthesized according to the previous works. Briefly, 10.0 g of urea powder and 20.0 mg of $Co(NO_3)_2 \cdot 6H_2O$ were dissolved distilled deionized water. After dried, the obtained compound was put into an aluminum–foil–wrapped crucible with a lid and heated in a muffle furnace in air from room temperature to 550 °C at a heating rate of 5 °C min^{-1} and maintained at this temperature for 2 h. After cooled, the obtained sample was washed several times with deionized water, dried and named as Co–CN–20. Similarly, sample Co–CN–10*,* Co–CN–30, and Co–CN–40 were synthesized in the same manner, but with 10.0, 30.0 and 40.0 mg of $Co(NO_3)_2 \cdot 6H_2O$ in the reaction, respectively. The g–C_3N_4 (CN) was obtained by the similar method but without the addition of $Co(NO_3)_2 \cdot 6H_2O$.

1.3 Synthesis of Co–N–C–*m*

240.0 mg Co–CN–*m* was dispersed in 90.0 mL deionized water and then 180.0

μL pyrrole (PY) was added. After ultrasound stirring for ~1.5 h, 6.0 mL 12.0 M HCl was added into the above suspension during agitation. Subsequently, 1.80 g $(NH_4)_2S_2O_8$ was slowly added under ice bath condition to initiate the polymerization of pyrrole. After 12 h, the black product polypyrrole (PPY)/Co–CN–*m* compounds were separated by centrifugation. The obtained PPY/Co–CN–*m* compounds were annealed under flowing N_2 at 900 °C for 2 h to get Co–N–co–doped carbon (Co–N–C–*m*). In addition, N–doped carbon (NC) was synthesized without the addition of Co–C–N–*m*, and was notated as Co–N–C–*m*. Similarly, N–doped multi-hole carbon (NMC) was also prepared using CN as a template.

1.4 Materials Characterization and Testing

1.4.1 Materials Characterization

The morphology and microstructure of the samples were measured by scanning electron microscope (FE-SEM, JEOL, JSM-6330f), transmission electron microscope (TEM, JEOL, JEM–2100) and high–angle annular dark–field STEM (HAADF–STEM, FEI Themis Z). The crystalline structure and defect nature of these samples were examined with X-ray diffraction (XRD, Rigaku, Ultima IV) and Raman spectroscopy (Jobin Yvon, Labram–010). Fourier transforminfrared spectroscopy (FTIR, Thermo Nicolet) decorated with an AVATAR 370 spectrometer and X–ray photoelectron spectroscopy (XPS) equipped with an ESCALAB250 XPS spectrometer were used to analyze the chemical composition of these samples. The specific surface area and pore structure of these samples were obtained on a surface area and pore size analyzer

(Micromeritics, ASAP 2020 HD) by recording the N_2 adsorption/desorption curves. Thermal gravimetric analysis (TGA) was recorded using a Rigaku standard TG-DTA analyzer (TG8121). The metal content of the Co–N–C–20 was analyzed by an iCAP 7600 ICP-OES instrument.

1.4.2 Electrochemical measurement

a. ORR performance

The electrochemical performance was tested in 0.1 M KOH electrolyte with a typical three-electrode system on a rotating disk electrode (RDE, Gamry Instruments, RDE 710). A platinum foil and Ag/AgCl electrode full of saturated KCl solution were adopted as auxiliary electrode and reference electrode, respectively. The working electrode was prepared as follows. 10.0 μL of 2.0 mg mL^{-1} dispersed sample ink was dropped onto a polished glassy carbon electrode (GCE, Φ=5 mm). Then, 6.0 μL of 0.050 *wt.*% Nafion solution was overlain on GCE to acquire the final working electrode. All potentials in this work was calibrated to reversible hydrogen electrode (RHE) by the equation: $E_{\text{RHE}} = E_{\text{Ag/AgCl}} + 0.97$ V in 0.1 M KOH electrolyte. Before ORR tests, the electrolyte saturated with N_2 or O_2 was realized by bubbling with pure N_2 or O_2 for at least 30 mins. Cyclic voltammetry (CV) was conducted in saturated N_2 or O_2 aura within the voltage range between 1.17 V and –0.03 V. Linear sweep voltammetry (LSV) was measured at a scanning rate of 10 mV s^{-1} within the voltage range between 1.05 V and 0.02 V at different rotation speeds from 400 to 1600 rpm. The ORR kinetic parameters were calculated with the typical Koutechy–Levich (K–L) equation[S1–S2]:

$$\frac{1}{J}=\frac{1}{0.62nFC_0D_0^{2/3}v^{-1/6}\omega^{1/2}}+\frac{1}{J_k} \tag{1}$$

where J represents tested current density, J_K is kinetic current density. n is electron transfer number, F refers to Faraday constant (96485 C mol^{-1}), C_0 is O_2 bulk concentration (1.2×10^{-3} M), D_0 stands for oxygen diffusion coefficient (1.9×10^{-5} cm^2 s^{-1}), v is electrolyte kinetic viscosity (0.01 cm^2 s^{-1}) and ω is disk angular velocity.

The H_2O_2 generation of the carbon samples was measured by rotating ring-disk electrode (RRDE-3A, ALS). The H_2O_2 yield (% H_2O_2) and electron transfer number were calculated with the following equations[S3]:

$$\%\ H_2O_2=\frac{200I_r/N}{(I_d+I_r/N)} \tag{2}$$

$$n=\frac{4I_d}{I_d+I_r/N} \tag{3}$$

Where I_d is disk current, I_r is ring current, N is current collection efficiency of the Pt ring (N=0.37) and n refers to the electron transfer number during ORR process.

Calculation of mass activity was done by the formula (A g^{-1}) = J/m, where J is the current density (mA cm^{-2}) at η = 0.75 V, and m is the mass loading of electroactive materials. Turnover frequency (TOF) (s^{-1}) = $JA/4nF$ with J as the current density (A cm^{-2}) at η = 0.75 V, n is the number of moles of the active sites, A is the geometrical surface area of the electrode, F is the faraday constant (96485.3 s A mol^{-1}) [S4-S5].

b. LIBs performance

Electrochemical measurements were implemented with standard two–electrode coin–cell (CR 2025). Cells were fabricated with lithium foil as the counter electrode, 1.0 M LiPF6 dissolved into the mixture solvent comprised of dimethyl carbonate/ethyl methyl carbonate/ethylene carbonate (1:1:1 by volume) as the electrolyte and Celgard 2500 as the separator. The working electrodes were prepared by mixing the active material (80 wt%), acetylene black (10 wt%), and polyvinylidene difluoride binder (10 wt%) in N–methyl–2–pyrrolidone, then coating the slurry uniformly coated on Cu foils and drying under vacuum at 80 °C for 12 h. The cells were assembled in an argon filled glovebox (the water and oxygen content were below 0.1 ppm). Cyclic voltammetry (CV) and electrochemical impedance spectroscopy (EIS) tests were conducted on an electrochemical workstation (Gamry Instruments, RDE 710). The EIS was measured at open circuit potential within the frequency range of 0.01–100 kHz, and CV was tested within the voltage range of 0.005–3.0 V. The galvanostatic charge/discharge curves were carried on a cell test system (Land CT2001 A) within the voltage range of 0.005–3.0 V at room temperature.

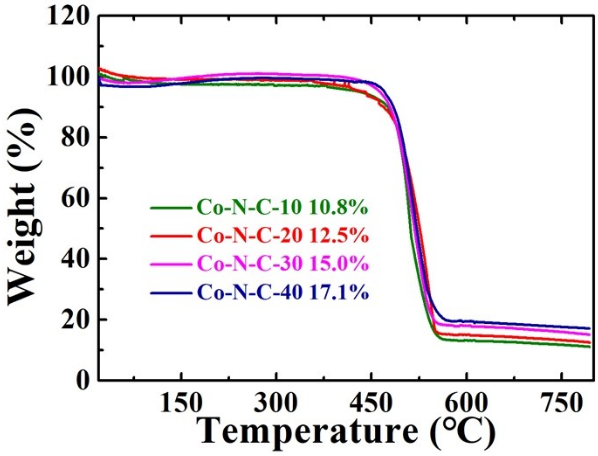

Fig. S1 TGA curves of Co–N–C–*m* in air from room temperature to 800 °C

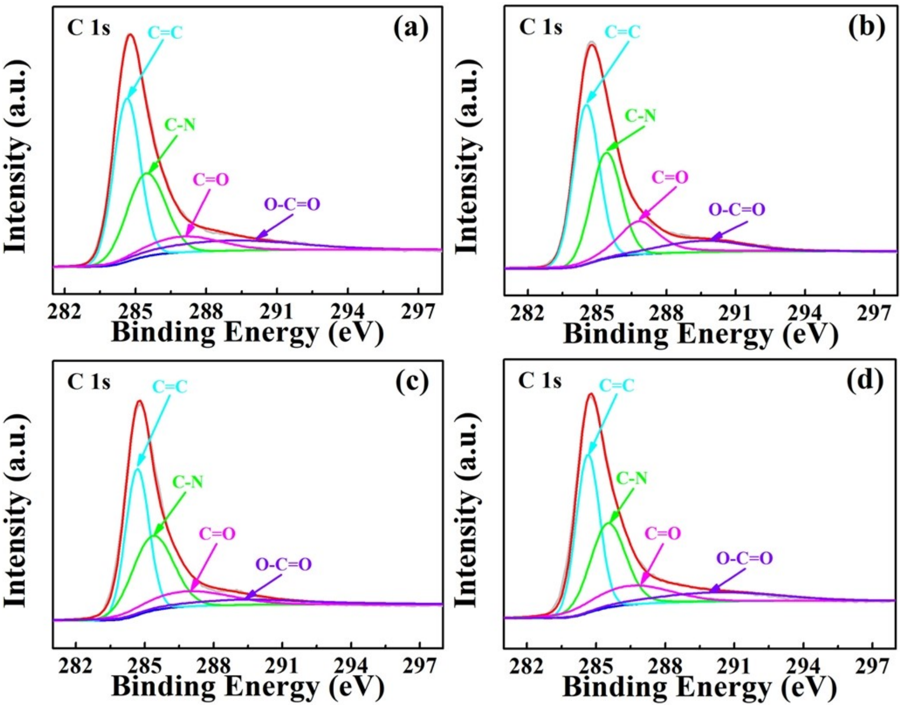

Fig. S2 High–resolution C 1*s* spectrum of NMC (a), Co–N–C–10 (b), Co–N–C–30 (c) and Co–N–C–40 (d)

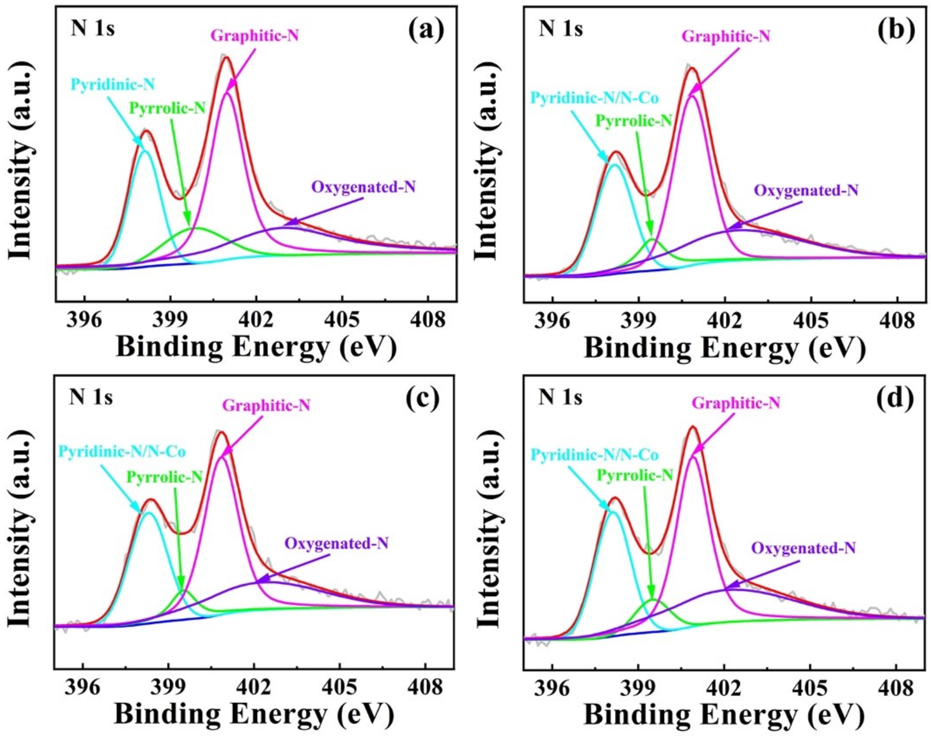

Fig. S3 High–resolution N 1*s* spectrum of NMC (a), Co–N–C–10 (b), Co–N–C–30 (c) and Co–N–C–40 (d)

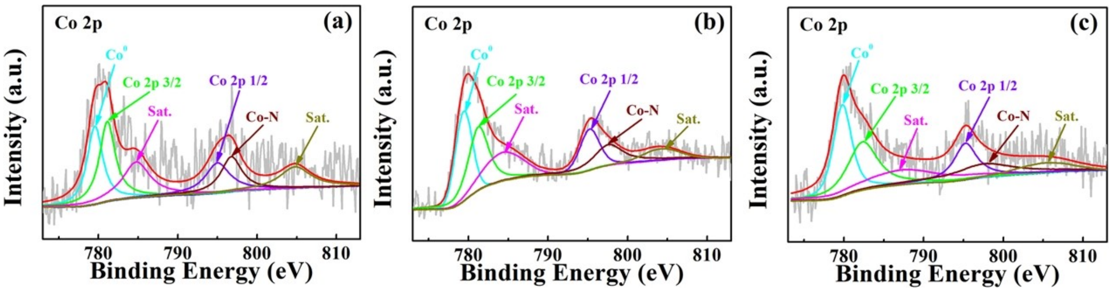

Fig. S4 High–resolution Co 2*p* spectrum of Co–N–C–10 (a), Co–N–C–30 (b) and Co–N–C–40 (c)

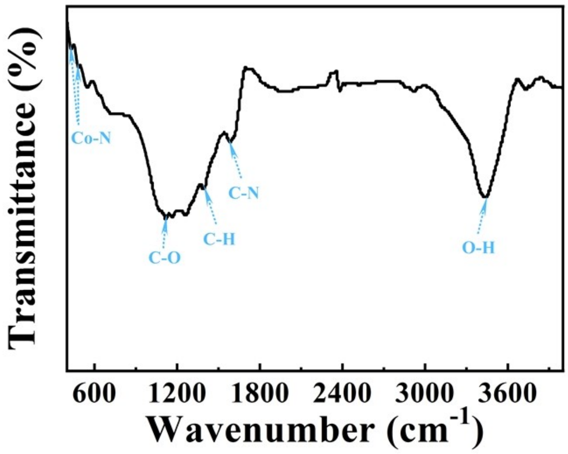

Fig. S5 FTIR spectra of Co–N–C–20.

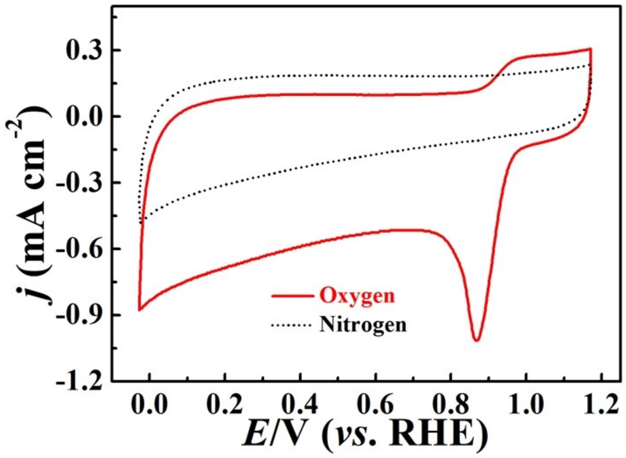

Fig. S6 CV curves on Co–N–C–20 electrode in oxygen and nitrogen saturated 0.1 M KOH electrolyte.

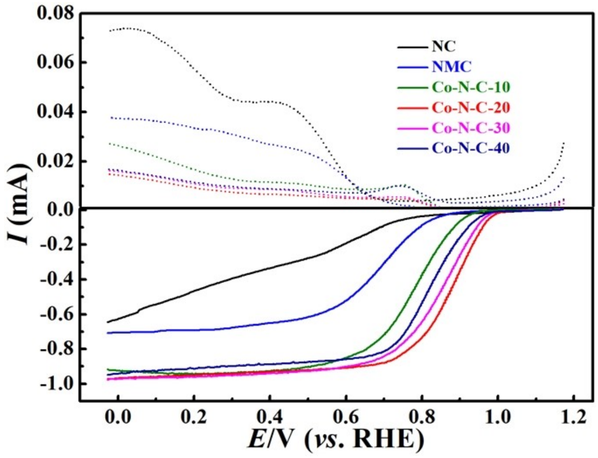

Fig. S7 LSV-RRDE profiles of NC, NMC and Co–N–C–*m* in O_2–saturated 0.1 M KOH.

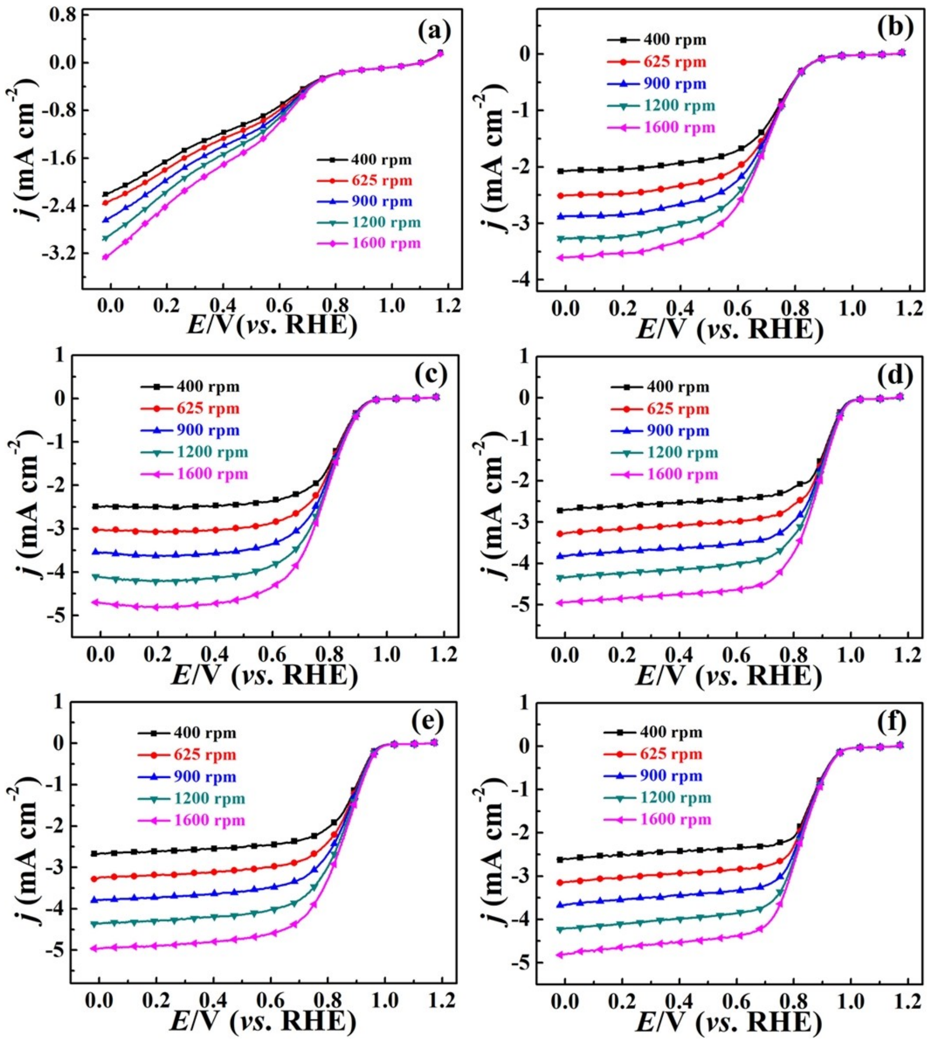

Fig. S8 LSV curves on NC (a), NMC (b), Co–N–C–10 (c), Co–N–C–20 (d), Co–N–C–30 (e) and Co–N–C–40 (f) electrodes at different rotation speeds in 0.1 M KOH electrolyte.

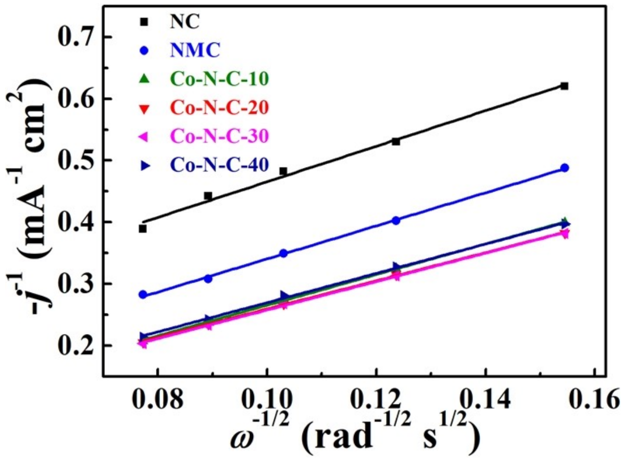

Fig. S9 K–L plots on NC, NMC and Co–N–C–*m* electrodes at various potentials in 0.1 M KOH electrolyte (d).

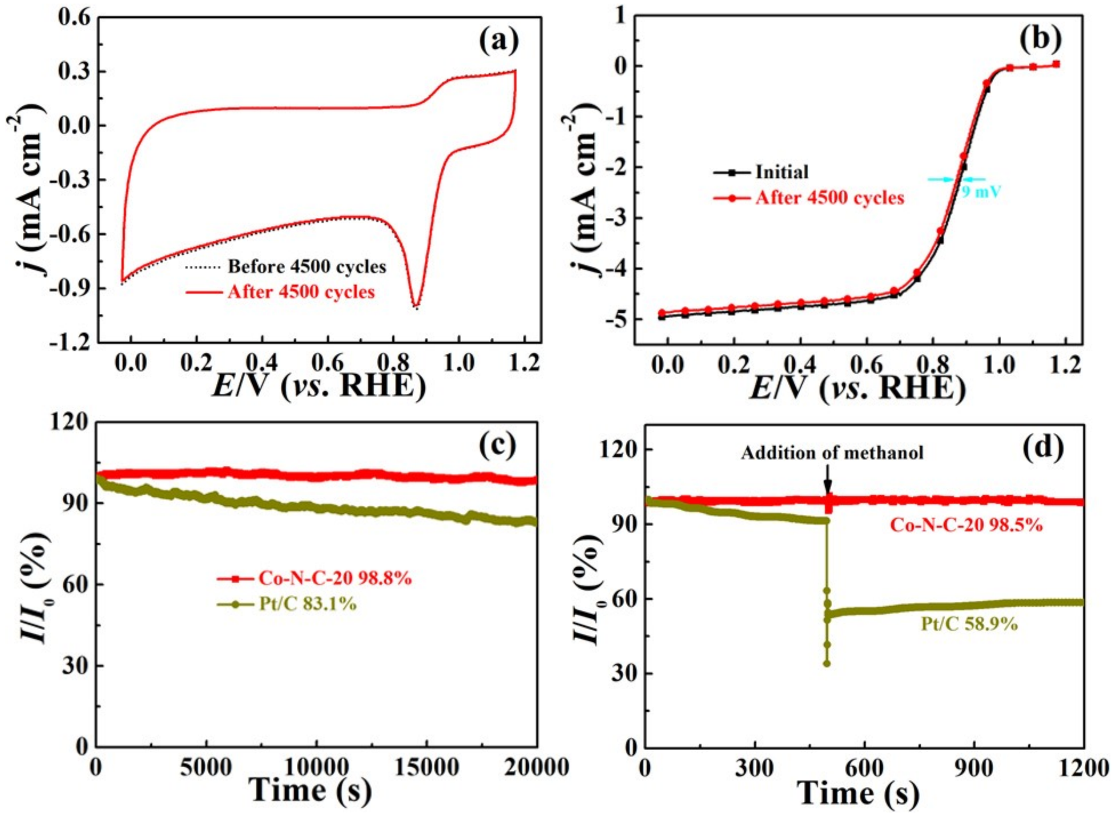

Fig. S10 CV curves on Co–N–C–20 electrode before and after 4500 continuous cycles in 0.1 M KOH electrolyte (a); LSV curves on Co–N–C–20 electrode at the rotation rate of 1600 rpm before and after 4500 continuous CV cycles in 0.1 M KOH (b); the *i*–*t* curves on Co–N–C–20 and commercialized Pt/C electrodes at 0.67 V for 20000 s in O_2 saturated 0.1 M KOH electrolyte (c); the *i*–*t* curves on Co–N–C–20 and commercialized Pt/C electrodes at 0.67 V in O_2 saturated 0.1 M KOH electrolyte before and after adding 3 M methanol (d).

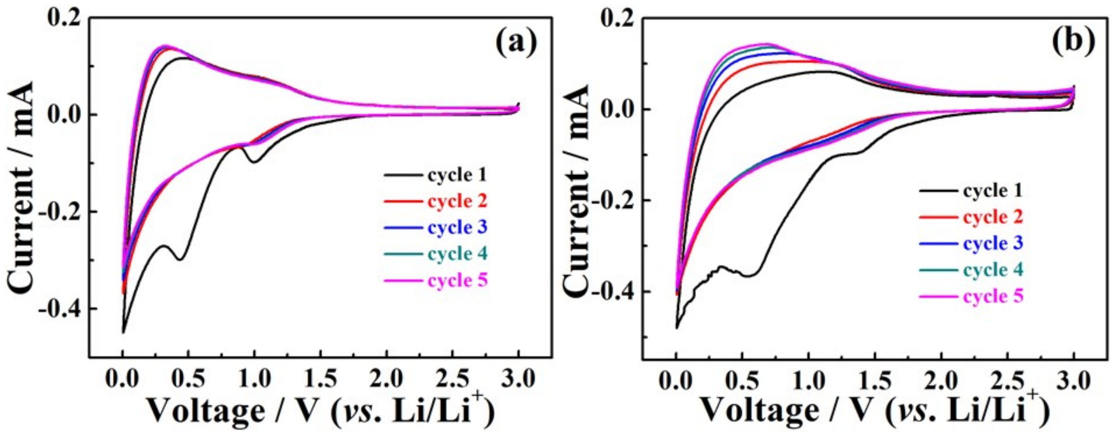

Fig. S11 CV curves of NC (a) and NMC (b) at 0.4 mV s^{-1}.

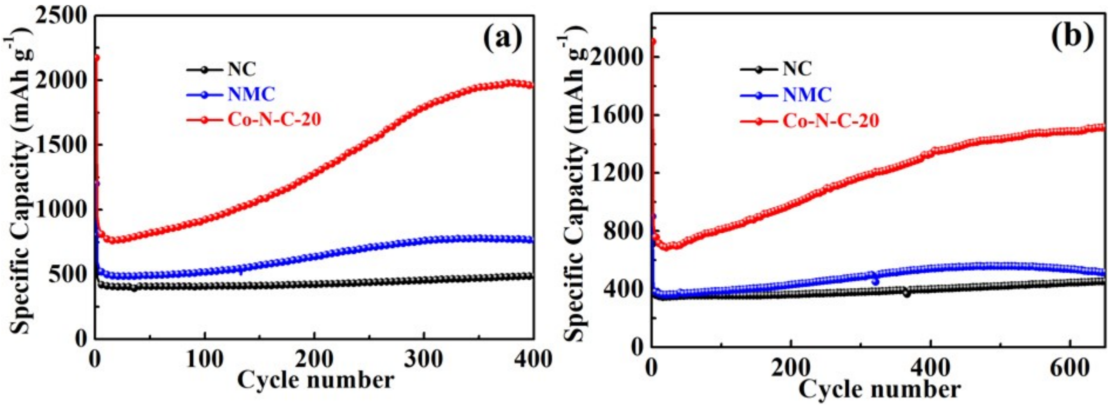

Fig. S12 Cycling performance at 0.5 (a) and 1 A g^{-1} (b) of the NC, NMC and Co–N–C–20, respectively.

Table S1 The specific BET result of NC, NMC and Co–N–C–20

Samples	Specific surface area (m^2/g)	pore volume (cm^3/g)	average pore width (nm)
NC	21.8	0.08	13.78
NMC	256.5	1.08	16.81
Co–N–C–20	317.3	1.39	17.50

Table S2 The XPS result of NMC and Co–N–C–*m*

Samples	C (*at.* %)	N (*at.* %)	O (*at.* %)	Co (*at.* %)
NMC	86.85	11.11	2.04	——
Co–N–C–10	86.01	11.20	2.53	0.26
Co–N–C–20	85.76	11.66	2.24	0.33
Co–N–C–30	85.42	11.47	2.71	0.40
Co–N–C–40	85.26	10.70	3.53	0.51

Table S3 The C 1*s* spectra fitting results of NMC and Co–N–C–*m*

Samples	C=C (%)	C–N (%)	C=O (%)	O-C=O (%)
NMC	43.05	31.84	11.66	13.45
Co–N–C–10	40.80	33.90	15.78	9.52
Co–N–C–20	39.29	36.19	12.82	11.69
Co–N–C–30	39.02	35.18	14.80	11.00
Co–N–C–40	38.89	31.33	16.74	13.04

Table S4 The N 1*s* spectra fitting results of NMC and Co–N–C–*m*

Samples	Pyridinic–N (%)	Pyrrolic–N (%)	Graphitic–N (%)	Oxygenated–N (%)
NMC	20.91	12.28	41.01	25.80
Co–N–C–10	24.97	8.40	41.43	25.20
Co–N–C–20	27.08	3.30	46.42	23.21
Co–N–C–30	26.91	6.66	42.22	24.21
Co–N–C–40	26.64	6.88	41.40	25.08

Table S5 The Co 2*p* spectra fitting results of Co–N–C–*m*

Samples	Co^0 (%)	Co $2p_{3/2}$ (%)	Sat. (%)	Co $2p_{1/2}$ (%)	Co–N (%)
Co–N–C–10	20.70	22.71	29.95	13.45	13.19
Co–N–C–20	25.11	22.67	23.80	13.48	14.94
Co–N–C–30	23.93	23.05	24.94	13.85	14.23
Co–N–C–40	23.18	24.92	24.20	13.99	13.71

Table S6 Comparison of ORR activity data for Co–N–C–*m* catalysts.

Catalysts	Mass activity (A g^{-1})	TOF (s^{-1})
Co–N–C–10	23.0	0.39
Co–N–C–20	42.1	0.62
Co–N–C–30	39.8	0.47
Co–N–C–40	38.7	0.42

Table S7. Comparison of the ORR performance between this work and some other works reported previously

Samples	Limiting current density (mA cm^{-2})	$E_{1/2}$ (V *vs.* *RHE*)	E_{onset} (V *vs.* *RHE*)	Electron transfer number (*n*)	loading mass (mg cm^{-2})	References
Co–N–C–20	**4.96**	**0.87**	**1.03**	**3.99**	**0.10**	**This work**
Single–holed Co/NC hollow particles	5.30	0.87	0.98	3.99	0.25	**[S6]**
Co/CoN$_x$/N–CNT/C	3.84	0.80	0.90	3.77	0.34	**[S7]**
Co–N–doped CFs	5.95	0.83	0.95	3.97	0.26	**[S8]**
Co–pyridinic N–C	5.30	0.87	0.99	3.99	0.25	**[S9]**
Co–N–C–900	4.20	0.80	0.92	3.70	0.20	**[S10]**
Co@NC/rGO–800	5.90	0.86	0.98	3.98	0.43	**[S11]**

Table S8. Comparison of the lithium storage properties between this work and some other works reported previously

Samples	Current density (mA g^{-1})	Cycle number (*n*)	Remaining capacity (mAh g^{-1})	References
Co–N–C–20	**2000**	**650**	**659**	**This work**
S-doped Co/N/C mesoporous nanorods	1000	500	624	**[S12]**
Co/CoN$_x$/N–CNT/C	1860 (5 C)	500	1091	**[S13]**
Co/NC–700	1000	1000	434	**[S14]**
3D rich Fe–N–C species	1860 (5 C)	400	400	**[S15]**
Ni@NC–rGO	1000	600	1047	**[S16]**
N–C@Co/Ni HDNCs	2000	500	323	**[S17]**

References

S1 Q. Shi, F. Peng, S. Liao, H. Wang, H. Yu, Z. Liu, B. Zhang, D. Su, Sulfur and nitrogen co-doped carbon nanotubes for enhancing electrochemical oxygen reduction activity in acidic and alkaline media, *J. Mater. Chem. A*, 2013, **1**, 14853–14857.

S2 Z. Y. Wu, X. X. Xu, B. C. Hu, H. W. Liang, Y. Lin, L. F. Chen, S. H. Yu, Iron carbide nanoparticles encapsulated in mesoporous Fe-N-doped carbon nanofibers for efficient electrocatalysis, *Angew. Chem.*, 2015, **127**, 8297–8301.

S3 C. Y. Chen, C. Tang, H. F. Wang, C. M. Chen, X. Y. Zhang, X. Huang, Q. Zhang, Oxygen reduction reaction on graphene in an electro-fenton system: in situ generation of H_2O_2 for the oxidation of organic compounds, *ChemSusChem*, 2016, **9**, 1194–1199.

S4 A. M. El-Sawy, I. M. Mosa, D. Su, C. J. Guild, S. Khalid, R. Joesten, J. F. Rusling, S. L. Suib Controlling the active sites of sulfur-doped carbon nanotube–graphene nanolobes for highly efficient oxygen evolution and reduction catalysis. *Adv. Energy Mater.*, 2016, **6**, 1501966.

S5 G. L. Tian, Q. Zhang, B. Zhang, Y. G. Jin, J. Q. Huang, D. S. Su, F. Wei, Toward full exposure of "active sites": Nanocarbon electrocatalyst with surface enriched nitrogen for superior oxygen reduction and evolution reactivity. *Adv. Funct. Mater.*, 2014, **24**, 5956–5961.

S6 B. Y. Guan, L. Yu, X. W. Lou, Formation of single-holed cobalt/N-doped carbon hollow particles with enhanced electrocatalytic activity toward oxygen reduction reaction in alkaline media, *Adv. Sci.*, 2017, **4**, 1700247.

S7 H. H. Zhong, Y. Luo, S. He, P. G. Tang, D. Q. Li, N. Alonso-Vante, Y. J. Feng, Electrocatalytic cobalt nanoparticles interacting with nitrogen-doped carbon nanotube in situ generated from a metal–organic framework for the oxygen reduction reaction, *ACS Appl. Mater. Inter.*, 2017, **9**, 2541–2549.

S8 C. Liu, J. Wang, J. S. Li, J. Z. Liu, C. H. Wang, X. Y. Sun, J. Y. Shen, W. Q. Han, L. J. Wang, Electrospun ZIF-based hierarchical carbon fiber as an efficient electrocatalyst for the oxygen reduction reaction, *J. Mater. Chem. A*, 2017, **5**, 1211–1220.

S9 Y. Ha, B. Fei, X. X. Yan, H. B. Xu, Z. L. Chen, L. X. Shi, M. S. Fu, W. Xu, R. B. Wu, Identifying the dominant role of pyridinic–N–Mo bonding in synergistic electrocatalysis for ambient nitrogen reduction, *Adv. Energy Mater.*, 2020, **10**, 2002592.

S10 T. Hao, C. Zhang, P. P. Su, Z. F. Shen, H. Liu, G. X. Wang, S. M. Liu, J. Liu, Metal–organic–framework–derived formation of Co–N–doped carbon materials for efficient oxygen reduction reaction, *J. Energy Chem.*, 2020, **40**, 137–143.

S11 C. Zhang, J. Liu, Y. X. Ye, Q. Chen, C. H. Liang, Encapsulation of Co-based nanoparticle in N-doped graphitic carbon for efficient oxygen reduction reaction, *Carbon*, 2020, **156**, 31–37.

S12 H. W. Liang, X. D. Zhuang, S. Bruller, X. L. Feng, K. Mullen, Hierarchically porous carbons with optimized nitrogen doping as highly active electrocatalysts for oxygen reduction, *Nat. Commun.*, 2014, **5**, 1–7.

S13 T. T. Guan, J. H. Zhao, G. L. Zhang, J. L. Wang, D. D. Zhang, K. X. Li, Emplate-free synthesis of honeycomblike porous carbon rich in specific 2–5 nm mesopores from a pitch–based polymer for a high–performance supercapacitor, *ACS Sustain. Chem. Eng.*, 2018, **7**, 2116–2126.

S14 L. Wang, Z. H. Wang, L. L. Xie, L. M. Zhu, X. Y. Cao, ZIF–67–derived N–doped Co/C nanocubes as high–performance anode materials for lithium-ion batteries, *ACS Appl. Mater. Inter.*, 2019, **11**, 16619–16628.

S15 C. M. Huang, J. Mahmood, J. K. Zhang, Z. H. Zhu, D. D. Chen, P. R. Chen, H. J. Noh, I. Ahmad, J. T. Xu, J. B. Baek, Iron encased organic networks with enhanced lithium storage properties, *Energy Storage*, 2020, **2**, e114.